Theor. Comput. Fluid Dyn. (2005) 19(5): 355–375
DOI 10.1007/s00162-005-0171-7

ORIGINAL ARTICLE

Boualem Khouider · Andrew J. Majda

A non-oscillatory balanced scheme for an idealized tropical climate model

Part II: Nonlinear coupling and moisture effects

Received: 28 August 2004 / Accepted: 5 May 2005 / Published online: 10 October 2005

Abstract We use the non-oscillatory balanced numerical scheme developed in Part I to track the dynamics of a dry highly nonlinear barotropic/baroclinic coupled solitary wave, as introduced by Biello and Majda (2004), and of the moisture fronts of Frierson et al. (2004) in the presence of dry gravity waves, a barotropic trade wind, and the beta effect. It is demonstrated that, for the barotropic/baroclinic solitary wave, except for a little numerical dissipation, the scheme utilized here preserves total energy despite the strong interactions and exchange of energy between the baroclinic and barotropic components of the flow. After a short transient period where the numerical solution stays close to the asymptotic predictions, the flow develops small scale eddies and ultimately becomes highly turbulent. It is found here that the interaction of a dry gravity wave with a moisture front can either result in a reflection of a fast moistening front or the pure extinction of the precipitation. The barotropic trade wind stretches the precipitation patches and increases the lifetime of the moisture fronts which decay naturally by the effects of dissipation through precipitation while the Coriolis effect makes the moving precipitation patches disappear and appear at other times and places.

Keywords Non-oscillatory balanced schemes · Barotropic-baroclinic nonlinear interactions · Precipitation fronts · Large scale equatorial waves

PACS 02.70.Bf; 02.30.Jr; 92.60.Bh; 92.60.Dj; 92.60.Jq

1 Introduction

It is argued in the introduction of Part I of this series of papers that simplified models with a crude vertical resolution are an important tool for the study of both lateral energy exchange between the tropics and the midlatitudes and for model parametrizations of tropical deep convection and convectively coupled waves, see [1–9] and [10–15] for references. Here we test and use the idealized model developed in Part I for the case of a dry equatorial solitary wave composed of two barotropic and baroclinic components, nonlinearly interacting with each other, and we use it to study the effect of moisture through the interactions of dry gravity waves, a barotropic trade wind, and the Earth's rotation with propagating precipitation fronts. The solitary wave solution was discovered by Biello and Majda [16] as a result of the resonant interactions of equatorial barotropic and baroclinic Rossby waves while the precipitation fronts were recently introduced by Frierson et al. [17] as a zero limiting solution for the linearized equatorial shallow water equations with moisture.

Communicated by R. Klein

B. Khouider (✉)
Mathematics and Statistics, University of Victoria, PO BOX 3045 STN CSC, Victoria, B.C., V8W 3P4, Canada
E-mail: khouider@math.uvic.ca

A. J. Majda
Department of Mathematics and Center for Atmosphere/Ocean Sciences, Courant Institute, New York University, 251 Mercer Street, New York, NY 10012, USA

Recall that our idealized model, discussed in Part I, carries a barotropic mode and a baroclinic mode interacting through highly non-linear terms and is augmented with a vertically integrated moisture equation to add the moisture effects in a fashion mimicking a tropical deep convective parametrization. The governing equations are summarized below for convenience.

$$\begin{aligned}\frac{\partial \overline{\mathbf{v}}}{\partial t} + \overline{\mathbf{v}} \cdot \nabla \overline{\mathbf{v}} + y\overline{\mathbf{v}}^{\perp} + \nabla \overline{p} &= -\frac{1}{2}\left(\mathbf{v} \cdot \nabla \mathbf{v} + \mathbf{v}\mathrm{div}\mathbf{v}\right) \\ &= -\frac{1}{2}\mathrm{div}\left(\mathbf{v} \otimes \mathbf{v}\right) \\ \mathrm{div}\overline{\mathbf{v}} &= 0, \end{aligned} \tag{1.1}$$

$$\begin{aligned}\frac{\partial \mathbf{v}}{\partial t} + \overline{\mathbf{v}} \cdot \nabla \mathbf{v} - \nabla\theta + y\mathbf{v}^{\perp} &= -\mathbf{v} \cdot \nabla \overline{\mathbf{v}} \\ \frac{\partial \theta}{\partial t} + \overline{\mathbf{v}} \cdot \nabla\theta - \mathrm{div}\mathbf{v} &= \mathcal{C} - Q_R \end{aligned} \tag{1.2}$$

and

$$\frac{\partial q}{\partial t} + \overline{\mathbf{v}} \cdot \nabla q + \tilde{Q}\mathrm{div}\mathbf{v} = -\mathcal{P} + E. \tag{1.3}$$

The equations in (1.1) through (1.3) constitute, respectively, an incompressible system for the barotropic waves and a (linear) shallow water system for the advected equatorial baroclinic waves, forced and coupled through highly nonlinear terms, plus a vertically integrated moisture equation, providing a closure for the deep convective-like heating forcing the baroclinic system. The equations in (1.1) and (1.2) are obtained by a Galerkin projection of the beta-plane primitive equations onto the barotropic and the first baroclinic modes. More discussions of these equations and their detailed derivation are found in Part I and [1]. Here $\bar{\mathbf{v}}$ is the barotropic velocity, $\bar{p}$ is the barotropic pressure, $\mathbf{v}$ is the first baroclinic velocity component, θ is the associated potential temperature, $\mathcal{C}$ is a deep convective-like heating, and Q_R is the radiative cooling. In (1.3), q is the vertically averaged moisture content with $\tilde{Q}$ the moisture stratification. The term $\mathcal{P}$ is the bulk precipitation rate while E is the surface evaporation rate.

Moreover, a fractional stepping–operator splitting algorithm for solving the coupled system formed by (1.1) and (1.2) was introduced in Part I. When the effects of moisture and radiation are ignored, $\mathcal{C} = Q_R = 0$, this system is decomposed into a linear subsystem for the advected equatorial baroclinic waves, an incompressible system for the barotropic flow, and a nonlinear ODE system gathering the interaction terms on the right hand sides of (1.1) and (1.2).

As in Part I, we consider a zonally oriented channel domain centered at the equator with periodic boundary conditions in the zonal variable x and no-flow boundary conditions at the North/South channel walls, $\mathbf{v}(x, y = \pm Y) = \bar{\mathbf{v}}(x, y = \pm Y) = 0$. Here Y is the distance of the walls from the equator which is fixed to $Y = 5,000$ km (unless otherwise specified) while the zonal period is set to $X = 40,000$ km, the Earth perimeter at the equator. It is particularly interesting to recall that, under the given boundary conditions, the dry system conserves energy in the absence of external forces and the three split subsystems conserve their own energies by design. More precisely, the baroclinic energy,

$$\mathcal{E}_C(t) = \frac{1}{4}\int_{-Y}^{Y}\int_{0}^{X} |\mathbf{v}|^2 + \theta^2 \,\mathrm{d}x\mathrm{d}y, \tag{1.4}$$

and the barotropic energy,

$$\mathcal{E}_T(t) \equiv \frac{1}{2}\int_{-Y}^{Y}\int_{0}^{X} |\overline{\mathbf{v}}|^2, \,\mathrm{d}x\mathrm{d}y \tag{1.5}$$

are conserved in the absence of the interaction terms on the right hand sides of (1.1) and (1.2) and $\mathcal{C} = Q_R = 0$ while the total dry energy

$$\mathcal{E}_d \equiv \mathcal{E}_C + \mathcal{E}_T \tag{1.6}$$

is conserved when $\mathcal{C} = Q_R = 0$. We will see in Sect. 3 that the whole system formed by (1.1), (1.2), and (1.3) dissipates energy through precipitation.

The advected baroclinic equations are discretized by the f-wave algorithm of Bale et al. [18] and the barotropic system is handled by the non-oscillatory central scheme of Levy and Tadmor [19] while the

decoupled ODE's are solved by a second order Runge-Kutta method. Recall that the f-wave method constitutes a non-oscillatory balanced scheme for hyperbolic systems with varying flux functions and source terms. The three systems communicate with each other in an overall fractional step–splitting procedure. Recall also that the f-wave algorithm and the central scheme are validated independently for the equatorial channel domain by using exact solutions, consisting of a variety of equatorial baroclinic waves and Rossby wave packets, respectively.

The remainder of the paper is organized as follows. In Sect. 2, the solitary wave solution of Biello and Majda [16] is formulated explicitly and used to initialize the dry system formed by (1.1) and (1.2) when $\mathcal{C} = Q_R = 0$. In other words, the overall time splitting strategy coupling the f-wave algorithm for the advected baroclinic waves, the central scheme for the barotropic flow, and the Runge-Kutta ODE solver for the interacting terms is tested for the first time. The results reported in Sect. 2 reveal that the overall scheme preserves total energy up to little numerical dissipation despite the highly non-linear interactions between the baroclinic and barotropic components of the wave. It is also demonstrated that the numerical solution stays close to the asymptotic predictions during a short transient period after which the flow develops small scale eddies and ultimately becomes highly turbulent.

In Sect. 3, we reintroduce the moisture equation into the system and consider some (exact) limiting solutions constructed recently by Frierson et al. [17] in the form of precipitation fronts. Namely, solutions for the linear one-dimensional shallow water equations with moisture forced by a convective heating-like relaxation scheme in the limit of zero relaxation time, for the simple case without rotation and without barotropic advection. The precipitation fronts consist of moving interfaces separating moist-saturated regions and dry-unsaturated regions. We then use these solutions to construct appropriate initial conditions to use the non-oscillatory balanced code for the case with moisture. Our setup consists of a moving and areally decaying moist region surrounded by two dry regions; *a dying moisture wave* (see Figs. 4 and 5 below). After the validation of our setup with a finite (non zero) convective time and the exploration of the interactions of dry gravity waves with the precipitation fronts, we gradually add the effect of advection by a trade-wind like barotropic wind, the effect of rotation (beta-effect), and then both rotation and barotropic advection. The results reported in Sect. 3 demonstrate that, in the simplest setup of no barotropic advection and no rotation, the interaction of a dry gravity wave with a moisture front can either result in a reflection of a fast moistening front or the pure extinction of the precipitation, depending on the strength and steepness of the wave itself. The barotropic trade wind serves to stretch the precipitation patch and increases the lifetime of the precipitation front, which decays naturally by the effects of dissipation through precipitation. The Coriolis effect makes the moving precipitation patches disappear and appear at other times and places in a highly chaotic and intermittent process, given the abundance of equatorial waves with which they can interact. A concluding discussion is given in Sect. 3 while the algorithm yielding the dying moisture wave–initial data of Sect. 3 is summarized in the Appendix at the end.

2 Nonlinear barotropic/baroclinic coupling

We use the overall algorithm obtained by coupling the schemes described in Sects. 4 and 5 of Part I via the interaction ODE system (Eq. (3.4) of Part I) via the Strang's fractional step procedure. This test particularly demonstrates the robustness of the code and its usefulness for studying the baroclinic-barotropic interactions near the equator. We use, for this purpose, an asymptotic (KdV-like) solution, to the coupled equations in (1.1) and (1.2), which was discovered recently by Biello and Majda [16], in the long-wave limit [20] where the zonal wavelength is assumed to be larger than the meridional wavelength of about 5400 km. This particular value for the meridional wavelength is dictated by a resonance condition which leads to a relationship between the meridional wavenumber of the barotropic Rossby wave and the meridional index of the baroclinic Rossby wave. The width of our channel is thus adjusted accordingly. For simplicity, we skip the details of the derivation of the solitary waves. The interested reader is referred to [16]. The solitary wave of Biello and Majda is given in the form

$$\overline{\psi}(x, y, t) = B(x, t) \sin(k_2 y)$$
$$u(x, y, t) = A(x, t) \left(D_{m-1} - \frac{1}{m+1} D_{m+1} \right)$$

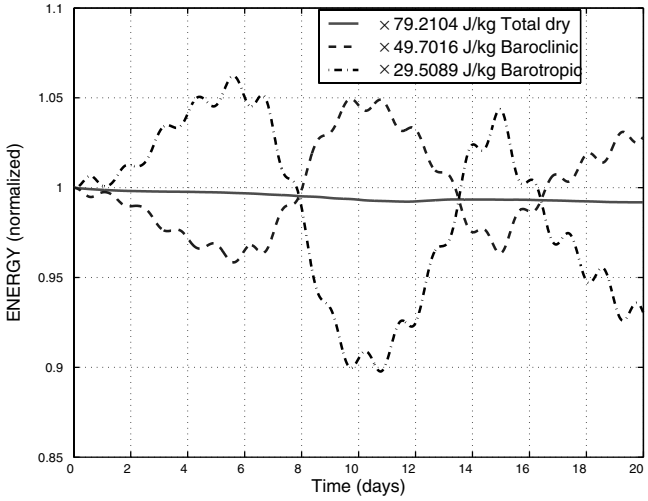

Fig. 1 Time history of the total (*solid*), the baroclinic (*dashed*), and the barotropic (*dash-dotted*) energies, normalized by their corresponding initial values, for the barotropic-baroclinic interacting solitary wave

$$v(x, y, t) = \frac{2\sqrt{2}}{2m+1}\frac{\partial A(x,t)}{\partial x}D_m$$
$$\theta(x, y, t) = A(x, t)\left(D_{m-1} + \frac{1}{m+1}D_{m+1}\right) \tag{2.1}$$

where the amplitude functions A and B, which solve a highly nonlinear dispersive PDE system in (x, t), are given by the formulas

$$A(x, t) = \bar{A} + \alpha\text{sech}^2(k_1(x - c_s t)); \quad B(x, t) = \bar{B} - \beta\text{sech}^2(k_1(x - c_s t))$$

with $\bar{A}$ and $\bar{B}$ are two closely related parameters which fix a mean barotropic wind at the equator, while α and β are two constants setting the wave amplitudes. The D_m's, $m = 1, 2$, are the parabolic cylinder functions [20, 21]. k_1 is the zonal wavenumber and $k_2 = \sqrt{2m+1}$ is the meridional wavenumber. In our simulation below we pick $m = 1$ and c_s a negative real number; the westward traveling speed of the solitary wave.

We run the fractional step algorithm, linking the three different routines as discussed above, with the initial data provided by the solitary wave in (2.1). We fix the parameters so that the mean barotropic wind at the equator blows eastward with a magnitude of 5 m/s and the zonal wavelength is on the order of 10,000 km. The resulting (total) wave speed of the solitary wave is $c_s = -23$ m/s. We use a resolution of 512×150 grid points, yielding approximately a mesh size of 75 km in each direction x and y, and a CFL = .9 based time step of about 15 minutes.

The history plots of the total (solid), the baroclinic (dashed), and the barotropic (dash-dotted) energies, normalized by their corresponding initial values, up to 20 days are shown in Fig. 1. In spite of the strong interactions between the two flow components during this long-time run, reflected by the auto-compensating ups and downs of the barotropic and baroclinic energies, the total energy is essentially preserved as should be the case, except for some small numerical dissipation becoming noticeable after about $t = 5$ days when some small scale structures start to develop. Nevertheless, this rather small diminishing in total energy with time is expected to decrease with grid refinement.

Also from Fig. 1 we can see that during the first two days or so the barotropic and baroclinic energies do not change much. This actually marks the time period during which the numerical solution remains fairly close to the asymptotic (initial) solution depicted in (2.1). In fact, in Fig. 2 we display both the baroclinic (left panels) and barotropic (right panels) flow structures by plotting the contours of the potential temperature, θ, for the baroclinic flow and those of the vorticity, $\overline{\omega}$, with the corresponding velocity profiles on top of them, for the asymptotic solution (E), in (2.1), and the numerical solution (N), obtained by the coupled code, at time $t = 2$ days.

Up to this time, the two solutions stay fairly close to each other both qualitatively and quantitatively. Especially, we notice that the two solutions are overall well aligned with each other, suggesting that the phase

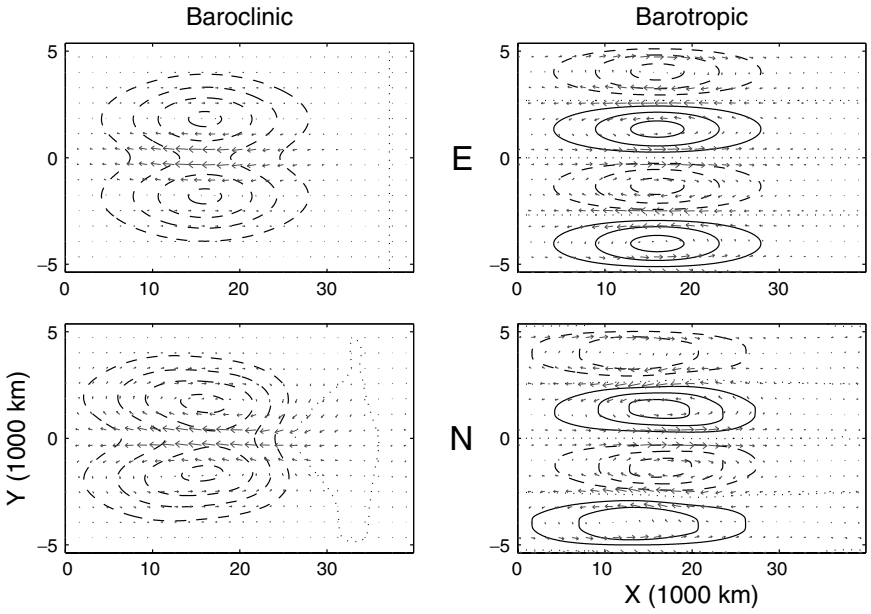

Fig. 2 Baroclinic and barotropic structure of the solitary wave at time $t = 2$ days. Comparison of the KdV-asymptotic solution (*top panels*) and the numerical solution (*bottom panels*). Contours of the potential temperature and those of the vorticity, respectively, with the corresponding velocity profiles overlaid. Contour interval 0.2. Solid: positive, Dash: negative, Dots: zero

speeds are in good agreement. However, we do see that the numerical (which provides an approximation to the full equations; with no asymptotics) deviates from its asymptotic analogue by showing a tilted oval shape at the center of the θ-contours on the left panel and a speed up of the front of the off equatorial vortices shown on the right bottom panel.

Figure 3 displays the flow structures (similarly to Fig. 2) of the numerical solution at times $t = 5.7, 11.5, 17$ days. Particularly apparent from the contours of θ, some small scale structures are starting to form at time $t = 5.7$ days, also we see that the two vortices which are closer to the equator are amplifying, thus, yielding very steep gradients. By the time $t = 11.5$ days, the original vortices are split on half, thus, transferring energy into small scales.

This energy cascade becomes even more visible at time $t = 17$ days and the numerical solution does no longer look like the original solitary wave. One plausible explanation for this bifurcation would be the shear instability which is associated with the sudden increase of the barotropic energy starting from time $t \approx 2$ days. The amount of energy permitting the increase of the barotropic energy is being extracted from the baroclinic flow (thanks to the energy conservation principle of the scheme) thus completely destroying the initial solitary wave structure. It is worth mentioning here that the barotropic mean profile utilized in the solitary wave exact solution in (2.1) is linearly unstable; however, the asymptotic theory [1, 16] allows a general, possibly linearly stable, barotropic shear, constrained to have only the same Fourier coefficient B for $\overline{\psi}$ from (2.1). While it is not important for us here, it would be interesting to see if such solutions are stable to be expected to occur in nature.

3 Effects of moisture

3.1 The convective relaxation scheme

Now we re-couple the equation for the vertically averaged moisture with a background gradient in (1.3) into the barotropic-baroclinic interaction equations in (1.1) and (1.2) via a simple convective parametrization-like relaxation scheme. Our goal is to test our non-oscillatory balanced scheme on the equations with moisture. Realistic convective parametrizations involve a large number of parameters and variables representing the different complex processes associated with the atmospheric convection such as the different cloud types, condensation and evaporation, radiative effects, etc. and would also likely invoke an active boundary layer [15, 22, etc.]. For the sake of simplicity, as in [17, 23] we use rather a simple relaxation scheme to parametrize

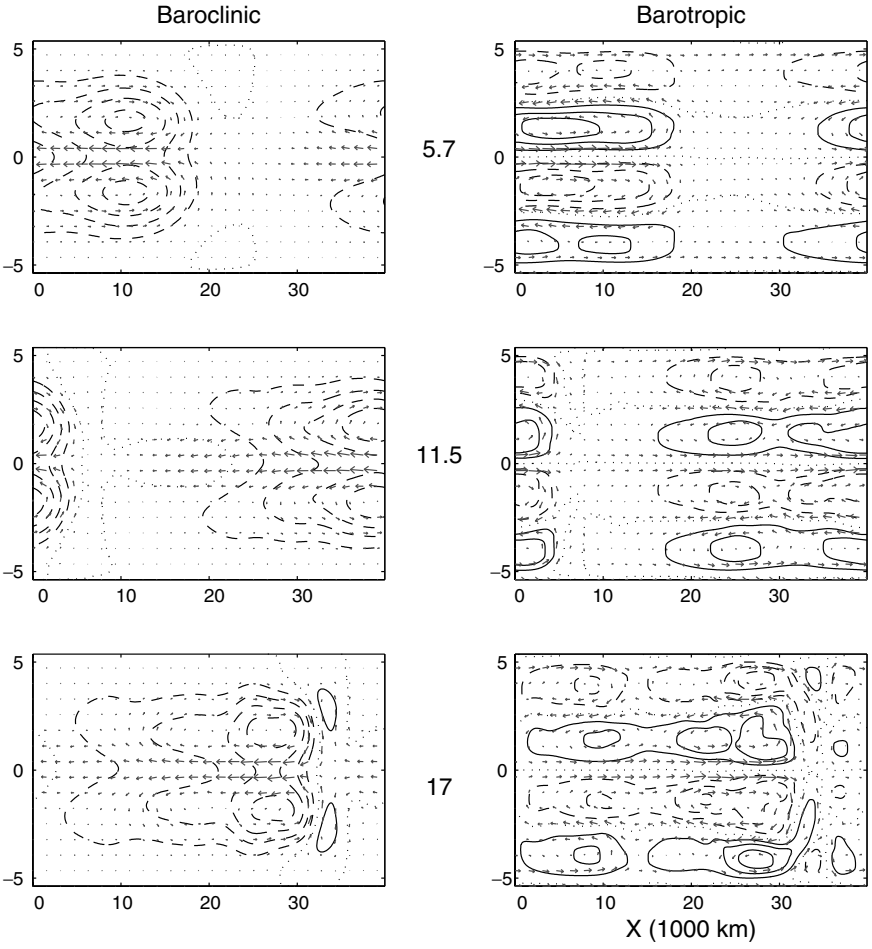

Fig. 3 Same as Fig. 2 but for the numerical solution at times $t = 5.7, 11.5, 17$ days

the precipitation rate, $\mathcal{P}$, which is set equal to the convective heating, $\mathcal{C}$, in (1.2). In order to access a certain family of exact solutions in the form of precipitation fronts, which have recently been discovered by Frierson et al. [17] and briefly summarized below, all the external forces, such as the sea-surface evaporation flux E, the momentum friction (not added to the equations), and the radiative cooling Q_R, are also ignored here, i.e., we set $E \equiv 0$, and $Q_R \equiv 0$ in (1.1) and (1.3). Nevertheless, it is argued in [17] that those terms do not affect much the dynamics of the moisture fronts on which we focus here. Namely, we consider the following barotropic-baroclinic system with a moisture relaxation scheme.

$$
\begin{aligned}
&\text{(A)} \quad \frac{\partial \overline{\mathbf{v}}}{\partial t} + \overline{\mathbf{v}} \cdot \nabla \overline{\mathbf{v}} + y \overline{\mathbf{v}}^{\perp} + \nabla \overline{p} = -\frac{1}{2} \mathrm{div}\,(\mathbf{v} \otimes \mathbf{v}) \\
&\text{(B)} \quad \nabla \cdot \overline{\mathbf{v}} = 0 \\
&\text{(C)} \quad \frac{\partial \mathbf{v}}{\partial t} + \overline{\mathbf{v}} \cdot \nabla \mathbf{v} - \nabla \theta + y \mathbf{v}^{\perp} = -\mathbf{v} \cdot \nabla \overline{\mathbf{v}} \\
&\text{(D)} \quad \frac{\partial \theta}{\partial t} + \overline{\mathbf{v}} \cdot \nabla \theta - \mathrm{div}\,(\mathbf{v}) = \mathcal{P} \\
&\text{(E)} \quad \frac{\partial q}{\partial t} + \overline{\mathbf{v}} \cdot \nabla q + \tilde{Q} \mathrm{div}\,(\mathbf{v}) = -\mathcal{P}.
\end{aligned}
\tag{3.1}
$$

The precipitation rate is parametrized according to the relaxation scheme

$$
\mathcal{P} = \frac{1}{\tau_c} (q - \tilde{q}(\theta))^{+} \tag{3.2}
$$

where $\tilde{q}(\theta)$, which measures a significant factor of the saturation value of environmental moisture, sets a moisture threshold beyond which the environment can sustain deep convection and hence produces precipitation. (Precipitation occurs only if the moisture content, q, exceeds the 'saturation' value, $\tilde{q}(\theta)$.) In (3.2) τ_c is a convective characteristic time which is fixed to $\tau_c = 2$ hours, see [17, 23] and

$$\tilde{q}(\theta) = \hat{q} + \alpha_c \theta \tag{3.3}$$

with α_c is a positive parameter and $\hat{q}$ is a fixed positive threshold constant. A relationship between α_c and $\tilde{Q}$ is obtained by imposing a fixed gravity wave speed, of 15 m/s, roughly consistent with observations [24], within the moist regions where $\mathcal{P} > 0$. This is done below. Versions of this "convective adjustment scheme" are often used in realistic general circulation models for climate; see [17, 23] for references.

3.2 Conservation of moist-equivalent potential temperature and moist gravity waves

When the radiative cooling and the surface evaporation are ignored, the equivalent potential temperature

$$\theta_e = \theta + q$$

satisfies the equation

$$\frac{\partial \theta_e}{\partial t} + \overline{\mathbf{v}} \cdot \nabla \theta_e - (1 - \tilde{Q}) \mathrm{div} \mathbf{v} = 0 \tag{3.4}$$

i.e., θ_e satisfies a divergence equation; therefore, it is conserved. As noted in [17], for rapid convective adjustments (small τ_c's), within the precipitation regions where $\mathcal{P} > 0$, we have

$$q = \hat{q} + \alpha_c \theta + O(\tau_c).$$

(Otherwise, $\mathcal{P}$ will explode when $\tau_c \longrightarrow 0$.) Therefore, (3.4) yields a new equation for the dry potential temperature, when $\tau_c \longrightarrow 0$,

$$\frac{\partial \theta}{\partial t} + \overline{\mathbf{v}} \cdot \nabla \theta - \frac{1 - \tilde{Q}}{1 + \alpha_c} \mathrm{div} \mathbf{v} = 0. \tag{3.5}$$

By substituting (3.5) to the θ-equation in (3.1) and gathering the momentum equations (3.1)(C), a new system of shallow water equations with gravity waves moving at a speed

$$c_m = \sqrt{\frac{1 - \tilde{Q}}{1 + \alpha_c}} \tag{3.6}$$

emerges. As in [17], we call these new waves 'moist gravity waves'. By relating c_m to the speed of observed convectively coupled Kelvin waves (e.g., [24]) which is about 15 m/s, the relationship in (3.6) links the parameters $\tilde{Q}$ and α_c when the moist gravity wave speed c_m is given. We use in our calculations the value $c_m = 15\,\mathrm{m/s}$. To close this equation and obtain plausible values for both $\tilde{Q}$ and α_c, we need to impose a value for the moisture gradient $\bar{Q}$. For a moisture gradient of $\bar{Q} = 1.49\,\mathrm{g\,kg^{-1}\,km^{-1}}$, and the hight of the troposphere of $H_T = 16\,\mathrm{km}$ (see Part I for details), we obtain

$$\tilde{Q} \approx .9 \implies \alpha_c \approx .025.$$

Still, we need to fix a value for the convective threshold, $\hat{q}$ in (3.3), for the moisture anomalies. By looking at Fig. 9.33 in Emanuel's book [25], we suggest the value $\hat{q} \equiv 2\,\mathrm{g/kg}$.

3.3 Dissipation of moist energy and entropy

We introduce the moist energy

$$\mathcal{E}_m(t) = \frac{1}{4}\int_0^X \int_{-Y}^Y \frac{(q+\tilde{Q}\theta)^2}{(1-\tilde{Q})(\alpha_c+\tilde{Q})}\,\mathrm{d}x\mathrm{d}y. \tag{3.7}$$

As discussed in [17], the total energy,

$$\mathcal{E} = \mathcal{E}_m + \mathcal{E}_d,$$

obtained by adding the moist energy in (3.7) to the dry energy introduced in (1.6), associated with the equations in (3.1), (3.2), and (3.3), satisfies the following equation,

$$\frac{\partial}{\partial t}\mathcal{E}(t) = -\frac{1}{2(\alpha_c+\tilde{Q})}\int_0^X \int_{-Y}^Y (q-\alpha_c\theta)\mathcal{P}\,\mathrm{d}x\mathrm{d}y \le 0. \tag{3.8}$$

Notice that $q \ge \hat{q} + \alpha_c\theta > \alpha_c\theta$, if $\mathcal{P} > 0$ which guarantees the energy dissipation in (3.8). Therefore, as pointed out in [17], the system in (3.1), (3.2), and (3.3), possesses a principle of energy dissipation via precipitation. Furthermore, it is shown in [17], by similar arguments, that, in the absence of the barotropic flow, the gradients of $\mathbf{v}$, θ and q also satisfy an energy principle where an $\mathcal{L}^2$-like norm involving $\nabla\mathbf{v}$, $\nabla\theta$, ∇q, namely the total energy for the gradient system, is similarly dissipated by precipitation. Therefore, the system in (3.1) will not develop (first order) discontinuities such as shocks during time integration. However, as we will see below, kinks in the level set contours of (i.e., discontinuities in the first derivatives of) $\mathbf{v}$, θ and q are permitted. Moreover, following [17], the moisture system in (3.1) possesses an entropy-like function given by $Z = q + \tilde{Q}\theta$, which is always decreasing along the trajectories of the barotropic flow. In fact, combining the equations (D) and (E) in (3.1) yields

$$\frac{\partial Z}{\partial t} + \overline{\mathbf{v}}\cdot\nabla Z = -(1-\tilde{Q})\mathcal{P} \le 0. \tag{3.9}$$

This equation will be used below to design a numerical scheme for the moisture system using the different methods discussed in Sects. 3–5.

3.4 Numerical solver for the moisture equation and its coupling into the barotropic-baroclinic interaction code

Now we incorporate the moisture equation into the barotropic-baroclinic interaction algorithm discussed in Sects. 3–5 to obtain a global solver for the equations with moisture in (3.1) with the precipitation rate, $\mathcal{P}$, given by the relaxation scheme described in (3.2) and (3.3). Since the Z-equation in (3.9) possesses a monotonicity principle and involves less terms than the q-equation in (3.1) (E), it is meaningful and more practical to use the former, instead of the latter, in (3.1).

We expand the fractional step scheme developed Part I and used in Sect. 2 to include the moisture equation. The forcing terms in (3.1) (D) and (3.9) are added to the interaction system in Eq. (3.4) of Part I which is augmented with an equation for θ and an other equation for Z accounting for the dynamics induced by the forcing terms on the right-hand side while the barotropic advection part of the Z-equation forms the fourth piece of the new algorithm. The following two systems are substituted/added into the global fractional step (Strang-splitting) strategy.

$$\begin{aligned}
\frac{\partial\overline{\mathbf{v}}}{\partial t} &= -\frac{1}{2}\mathrm{div}\,(\mathbf{v}\otimes\mathbf{v}) - c_d\overline{\mathbf{v}}\\
\frac{\partial\mathbf{v}}{\partial t} &= -\mathbf{v}\cdot\overline{\mathbf{v}} - c_d\mathbf{v}\\
\frac{\partial\theta}{\partial t} &= \mathcal{P} - Q_R\\
\frac{\partial Z}{\partial t} &= -(1-\tilde{Q})\mathcal{P} + E\\
\mathrm{div}\overline{\mathbf{v}} &= 0
\end{aligned} \tag{3.10}$$

and

$$\frac{\partial Z}{\partial t} + \bar{\mathbf{v}} \cdot \nabla Z = 0. \tag{3.11}$$

The discretization of (3.11) combines the predictor-corrector method in time and the NT scheme of Sect. 5 while the algorithm for solving (3.10) remains essentially the same as described in Sect. 3.2 except for the addition of the new forcing terms and the new equations for θ and Z. (The forcing terms E, Q_R and the frictional drag coefficient c_d are set to zero during the numerical tests described below, we included them in (3.10) for the sake of illustration only.)

3.5 Limiting dynamics and precipitation fronts

In this section we consider a simplified version of the equations in (3.1), reduced mainly to one space dimension with no barotropic advection, in the limit of small convective adjustment times, $\tau_c \longrightarrow 0$. We recall some interesting solutions recently introduced by Frierson et al. [17], in the form of propagating *precipitation fronts* separating dry-unsaturated and saturated-precipitating regions. Below we will interchangeably use the adjectives moist and dry versus the adjectives saturated and unsaturated. We then use these limiting solutions to define initial conditions for our full two-dimensional model in (3.1). Particularly, we investigate the beta-effect and the effect of the advection by a barotropic trade wind-like flow on the precipitation fronts.

The detailed discussion leading to the construction of the precipitation fronts is given in [17]. Next we give a brief summary for convenience. We consider the one-dimensional system involving only u, θ and q.

$$\begin{aligned} &\text{(A)} \quad \frac{\partial u}{\partial t} - \frac{\partial \theta}{\partial x} = 0 \\ &\text{(D)} \quad \frac{\partial \theta}{\partial t} - \frac{\partial u}{\partial x} = \mathcal{P} \\ &\text{(E)} \quad \frac{\partial q}{\partial t} + \tilde{Q}\frac{\partial u}{\partial x} = -\mathcal{P} \end{aligned} \tag{3.12}$$

with

$$\mathcal{P} = \frac{1}{\tau_c}(q - \hat{q} - \alpha_c\theta)^+.$$

It is established by Frierson et al. [17] that in the limit of $\tau_c \longrightarrow 0$, the simplified moisture equations in (3.12) admit three groups of simple solutions on the from of propagation fronts with jumps in the precipitation, $\mathcal{P}$, separating moist regions with $\mathcal{P} > 0$ and dry regions where $\mathcal{P} = 0$. They are continuous piecewise linear solutions, (u, θ, q), with jumps in their first derivatives, (u_x, θ_x, q_x), at the interface between moist and dry regions. In the limit of $\tau_c \longrightarrow 0$, the convective system adjusts quickly so that to leading order we have $(q = \hat{q} + \alpha_c\theta)$ within the moist regions. Therefore, in this limit, the moist and dry regions are characterized by [17]

$$\begin{aligned} &\text{Dry region: } \mathcal{P} = 0 \iff q < \hat{q} + \alpha_c\theta \text{ or } q = \hat{q} + \alpha_c\theta \text{ and } \tfrac{\partial q}{\partial t} < 0 \\ &\text{Moist region: } \mathcal{P} > 0 \iff q = \hat{q} + \alpha_c\theta \text{ and } \tfrac{\partial q}{\partial t} > 0. \end{aligned} \tag{3.13}$$

The exact solutions with the form of moving precipitation fronts for the the simplified system in (3.12) at the limit $\tau_c \longrightarrow 0$ are given below in terms of the jumps in the derivatives, u_x, θ_x, q_x, at the interface. First, the Rankine-Hugoniot jump conditions are written [17]

$$\begin{aligned} s[w] &= [\theta_x] \\ s[\theta_x] &= [w] - [\mathcal{P}] \\ s[q_x] &= -\tilde{Q}[w] + [\mathcal{P}] \end{aligned} \tag{3.14}$$

where $[f] = f^+ - f^-$ is the jump in f at the interface located at $x = 0$ with $f^\pm \equiv f(0^\pm)$ and $w \equiv -u_x$ is the vertical velocity (rescaled by a factor of $\frac{\pi L}{H_T}$) while s is the speed of the moving precipitation front. For simplicity we assume that at time $t = 0$ the moist region is the entire half real line with $x > 0$ while $x < 0$

defines the dry region. Therefore, since the precipitation is positive in the moist region and identically zero in the dry region we have

$$[\mathcal{P}] = \mathcal{P}^+ = \frac{\alpha_c + \tilde{Q}}{1+\alpha_c} w^+, \tag{3.15}$$

by using (3.12) on the moist side together with the conditions in (3.13). Notice that the positivity of $\mathcal{P}^+$ implies that $w^+ > 0$. In addition we have

$$q_x^+ = \alpha_c \theta_x^+, \; q_x^- \geq \alpha_c \theta_x^-, \quad \text{and} \quad q(0) = \hat{q} + \alpha_c \theta(0). \tag{3.16}$$

The most left equality in (3.16) follows directly from (3.13), the middle one expresses the fact that $q - \hat{q} - \alpha_c \theta$ is a non-decreasing function of $x < 0$ so that the region on the left of the interface remains dry, and the most right condition follows from a continuity argument. Combining the jump conditions in (3.14) with the constraints in (3.15) and (3.16) leads to the following set of solutions [17]

$$\begin{aligned} s &= \pm \left(1 - \frac{\alpha_c + \tilde{Q}}{1+\alpha_c} \frac{w^+}{[w]}\right)^{1/2} \\ [\theta_x] &= s[w] \\ [q_x] &= \left(\frac{1-\tilde{Q}}{s} - s\right)[w]. \end{aligned} \tag{3.17}$$

The equations in (3.17) form a parameter family of solutions to the convective system in (3.12) under the constraints in (3.15) and (3.16). Furthermore, in order to get a real valued propagation speed, one of the following conditions is required

$$w^- \leq \left(1 - \frac{\alpha_c + \tilde{Q}}{\alpha_c + 1}\right) w^+ \text{ or } w^- \geq w^+ > 0.$$

Therefore, according to Frierson et al. [17], the following three groups of precipitation fronts are possible.

– Drying fronts with the interface moving toward the moist region at a speed s such that

$$c_m \leq s \leq 1$$

where c_m is the moist gravity wave speed introduced above. (Recall that the dry gravity wave speed is the unity here.)

– Slow moistening fronts with the interface moving toward the dry region at a speed satisfying

$$-c_m \leq s \leq 0.$$

– Fast moistening fronts with speeds satisfying

$$s \leq -1.$$

Although only the drying fronts satisfy the Lax stability criterion for moving fronts [17, 26, 27], somewhat surprisingly all the three groups of precipitation fronts are successfully demonstrated, by numerical simulations in [17], to persist for small but reasonably finite adjustment times τ_c of a few hours. In our simulations below we pick $\tau_c = 2$ hours as utilized for example in [23].

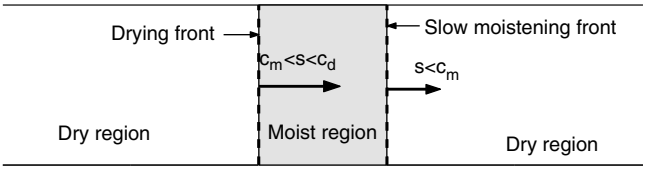

Fig. 4 Sketch of the *dying moisture wave*: two interfaces separating the dry regions and the moist (*shaded*) region. They are moving in the same direction with different speeds (*slow moistening and drying fronts*). The thick arrows represent the direction and magnitude, s, of the front speeds

3.6 Dying moisture wave

Our setup for numerical simulation using the equations with moisture in (3.1) consists on the design of a *dying moisture wave* by the aid of the precipitations fronts of Frierson et al. [17] discussed above. Recall our computational channel-domain covers the equatorial belt $[0, X] \times [-Y, Y]$ where X is the perimeter of the earth at the equator and Y is the distance of the channel walls from the equator. We divide this domain perpendicular to the equator into three regions: two dry regions on the zonal edges of the domain and a moist region in the middle. We then have two moist-dry interfaces. We design a dying-moisture-wave structure by inserting a slow moistening front at the right interface making the moist region move toward the dry region on the right and a drying front on the left interface to move the other dry region toward the moist region in the middle, see Fig. 4. Notice that the two interfaces are moving in the same direction, to the right; hence, the whole structure is moving in that direction but since the drying front is moving faster than the slow moistening front we expect the moist region to die out in a finite time. This is why we call it a *dying moisture wave*.

By imposing the constraints listed in the previous section on both interfaces a detailed algorithm for the construction of the dying-moisture-wave is given in Appendix B. In particular, we have the same-identical solution within the moist region satisfying the constraints imposed on both interfaces. The initial width of the moist region is 10,000 km, i.e., one fourth of the total domain width. Next, we discuss the results obtained by the moisture-scheme using the dying moisture wave as initial condition for the following cases. First, we start with the simplest case with no rotation and no barotropic advection, where we investigate both the effect of a finite but small τ_c on the precipitation fronts and their interactions with dry gravity waves. Then we gradually add the effect of the advection by a barotropic trade wind, the beta effect, and finally both the advection and the rotation together.

3.7 Validation with $\tau_c = 2$ hours and interaction with dry gravity waves

Here we run the simplified one-dimensional system in (3.12) with the initial condition in Fig. 4. (Actually, we have a two-dimensional flow in the x-z plane through the one-vertical baroclinic mode approximation with the vertical velocity w given via the divergence constraint.) Our aim is to investigate the effects of a finite adjustment time for the typical value of $\tau_c = 2$ hours on the dying-moisture-wave which is in theory a solution at the limit $\tau_c \longrightarrow 0$. In Fig. 5, we plot the contours of the zonal velocity u together with the color filled contours of the precipitation rate, $\mathcal{P}$, on top of them in the x-t plane (longitude-time). The dashed lines represent the position of the precipitation fronts associated with the drying and slow-moistening fronts as predicted by the limiting analysis.

The agreement between the asymptotic theory and the numerics with the finite $\tau_c = 2$ hours is well established, in Fig. 5, and the scenario of the dying-moisture-wave is reproduced with a good accuracy. However, in order to achieve this, we had to give up the natural periodic boundary conditions in x and use instead a linear extrapolation expanding the limiting solution beyond the boundaries. Indeed, periodic boundary conditions at $x = 0, X$ introduce a jump in the initial conditions from which two opposite dry gravity waves emerge. It turns out that the interaction of the dry gravity waves with the moisture fronts lead to interesting dynamics of wave interaction and reflection for the precipitation fronts.

As depicted in Fig. 6, the eastward gravity wave emanating from $x = 0$ at $t = 0$ (following the cusps in the zonal velocity contours on the left of the color-filled precipitation region, a rarefaction wave), which is weaker but closer to the precipitation wave, first hits the drying front at around time $t = 3.5$ days. At this time, a fast moistening front is reflected and propagates backward to the west at a speed larger than 50 m/s (compare to the shock wave on the right, which propagates at 50 m/s; this is a fast moistening front). The

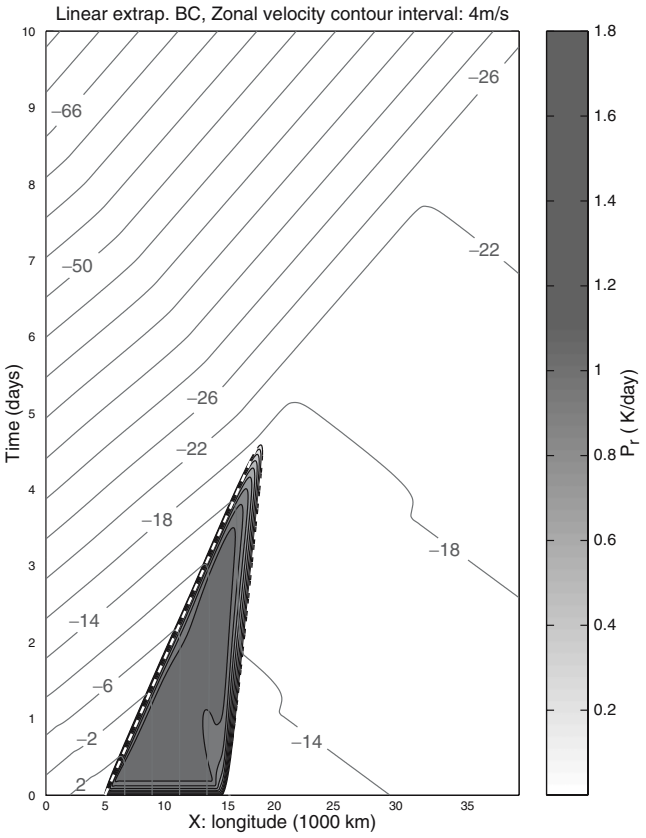

Fig. 5 Validation of the dying moisture wave with $\tau_c = 2$ hours, linear extrapolation boundary conditions at $x = 0, X$. Contours of zonal velocity, u, color-filled contours of precipitation, and position of the drying and slow-moistening fronts, as predicted by the theory [17], moving at 32.5 m/s and 7.5 m/s (*dash and dash-dot lines*), respectively

second propagating gravity wave emanating from $x = X$ at $t = 0$ is characterized by the steep gradient region (called "a shock wave") is propagating to the west toward the moving precipitation area. When the shock wave hits the moist region no fronts are reflected, instead it penetrates inside (like a dry intrusion) and dries out the whole structure while the reflected fast moistening front dies out after having traveled a distance of about 10,000 km. This last feature is perhaps due to the dissipation of energy by precipitation in (3.8).

3.8 Effect of the advection by a barotropic trade wind

Now, we add the trade wind-like barotropic flow, $\overline{\mathbf{v}} = (\overline{u}, \overline{v})$,

$$\overline{u} = -u_0 \cos\left(\frac{3\pi y}{Y}\right), \quad \overline{v} = 0 \tag{3.18}$$

with $u_0 = 5$ m/s, depicted in Fig. 7, to the equations in (3.1) (C), (D) and (E). We ignore the rotation effect, $\beta = 0$, the barotropic dynamics governed by (A) and (B), and the baroclinic-barotropic interaction terms on the right hand side of (C). We set the initial conditions to the dying moisture wave in x modulated by the cosine function in y to avoid a jump at the boundaries $y = \pm Y$. A truncation of the data by Dirichlet boundary conditions at $y = \pm Y$, would induce other dry gravity waves traveling in the north-south direction and may render the simulation very complex. We keep the the periodic boundary conditions in x in spite of the dry gravity waves emanating from the induced discontinuity, because otherwise (with the linear boundary conditions in x) the barotropic advection induces overwhelming growth which causes blowup.

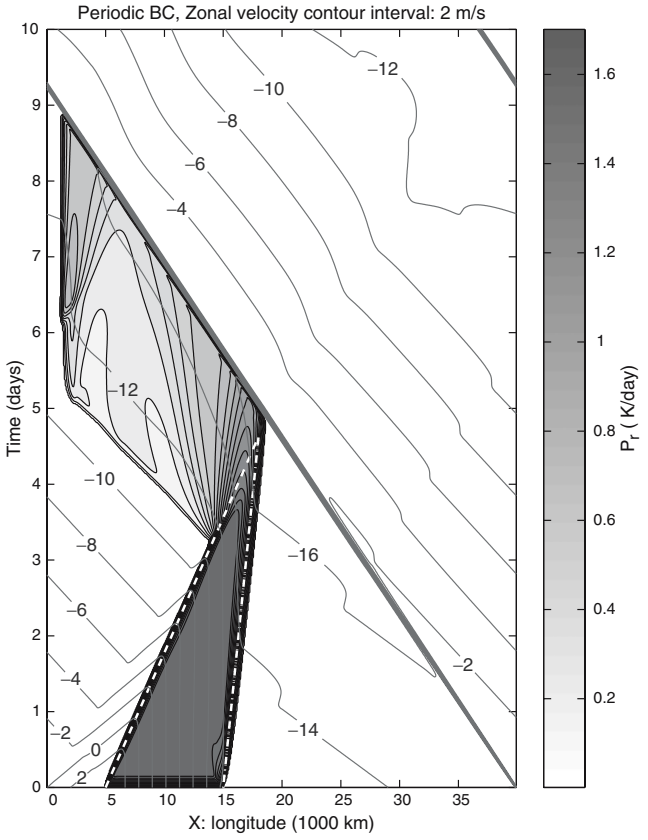

Fig. 6 Same as Fig. 5 but with periodic boundary conditions at $x = 0, X$. An eastward (*rarefaction*) and a westward (shock) dry gravity waves are created by the jump at $x = 0, X$ caused by the periodic boundary conditions

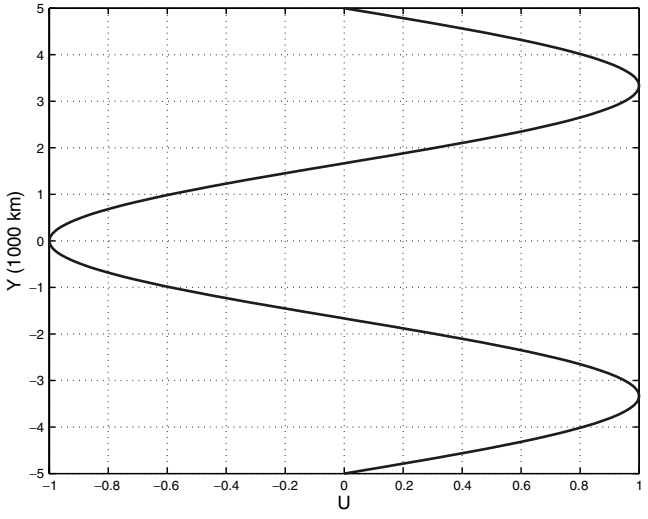

Fig. 7 Barotropic trade wind

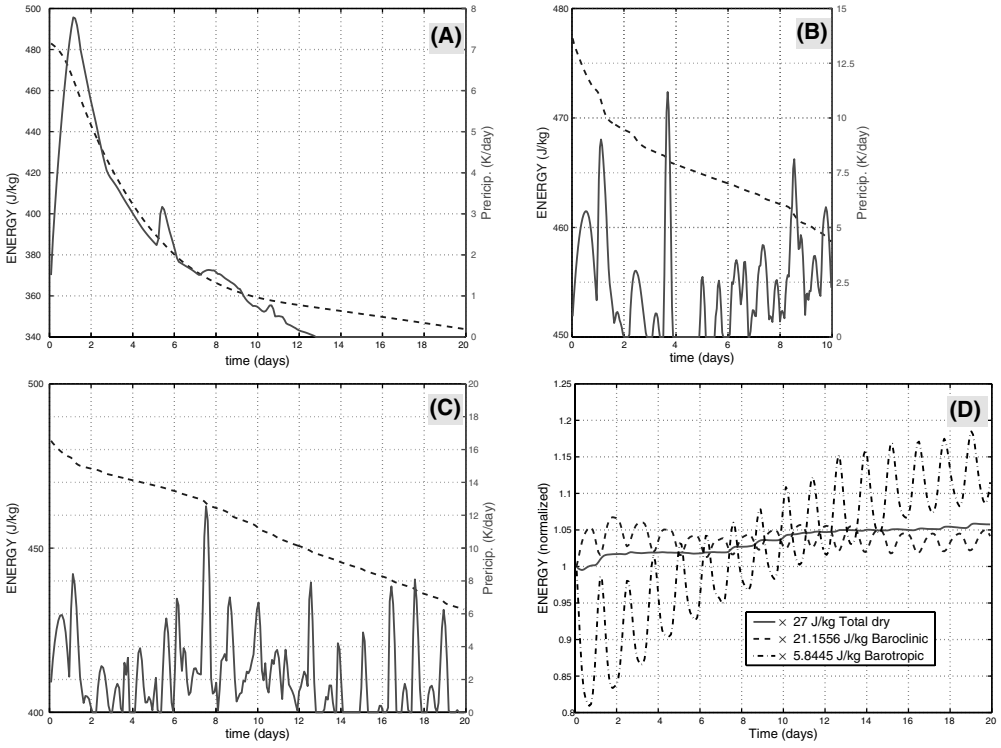

Fig. 8 History of total (*dry+moist*) energy (*dashed*) and precipitation rate (*solid*) for the dying moisture wave experiment: **A** with a trade wind barotropic advection, **B** with beta effect, and **C** with both barotropic advection and beta effect. The panel **D** displays the time histories of the total dry energy (*solid*) and the baroclinic (*dash*) and barotropic (*dash-dot*) contributions for the case in **C**

The initial condition for this test is therefore given by

$$\begin{aligned} u(x, y, 0) &= \cos\left(\frac{\pi y}{2Y}\right) u_l(x) \\ v(x, y, 0) &= 0 \\ \theta(x, y, 0) &= \cos\left(\frac{\pi y}{2Y}\right) \theta_l(x) \\ q(x, y, 0) &= \cos\left(\frac{\pi y}{2Y}\right) q_l(x) \end{aligned} \tag{3.19}$$

where u_l, θ_l, q_l is the piecewise linear limiting solution representing the dying moisture wave in Fig. 4.

The histories of both the total (dry + moist) energy in (3.7) and the precipitation rate are plotted in Fig. 8A. Perhaps, the most interesting thing we notice from Fig. 8A is that, unlike the case without barotropic advection in Fig. 6, the precipitation survives beyond the nine days time period. Notice the significant dissipation of total energy which ceases around $t = 13$ days when the precipitation becomes zero. This indeed confirms the dissipation of energy by precipitation as stated above. The longitude-latitude (x-y) contours of the water content, q, and the color filled contours of the precipitation rate, $\mathcal{P}$, at times $t = 0, 1, 3, 6, 9, 13$ days are plotted in Fig. 9. Already at time $t = 1$ day, at some distance away from the equator where the barotropic wind blows eastward, i.e., in the same direction as the moving moisture wave, the precipitation disappears. It becomes concentrated at the equator, which explains the first increase of the precipitation maximum on Fig. 8A.

As the precipitation front, confined to the equator, is trying to make its way forward in the eastward direction, as it would do in the absence of the barotropic advection, the trade wind, which blows westward at the equator, is pushing it backward to the west. This double effect stretches the moist region and expands it from 10,000 km to about 20,000 km wide at time $t = 1$ day. The effect of the eastward (rarefaction) wave emanating from the boundary conditions and moving eastward, as noted above, is suspected to be responsible for the formulation of the bowling pin-like shape located at time $t = 1$ day, around $x = 4300$ km (which is

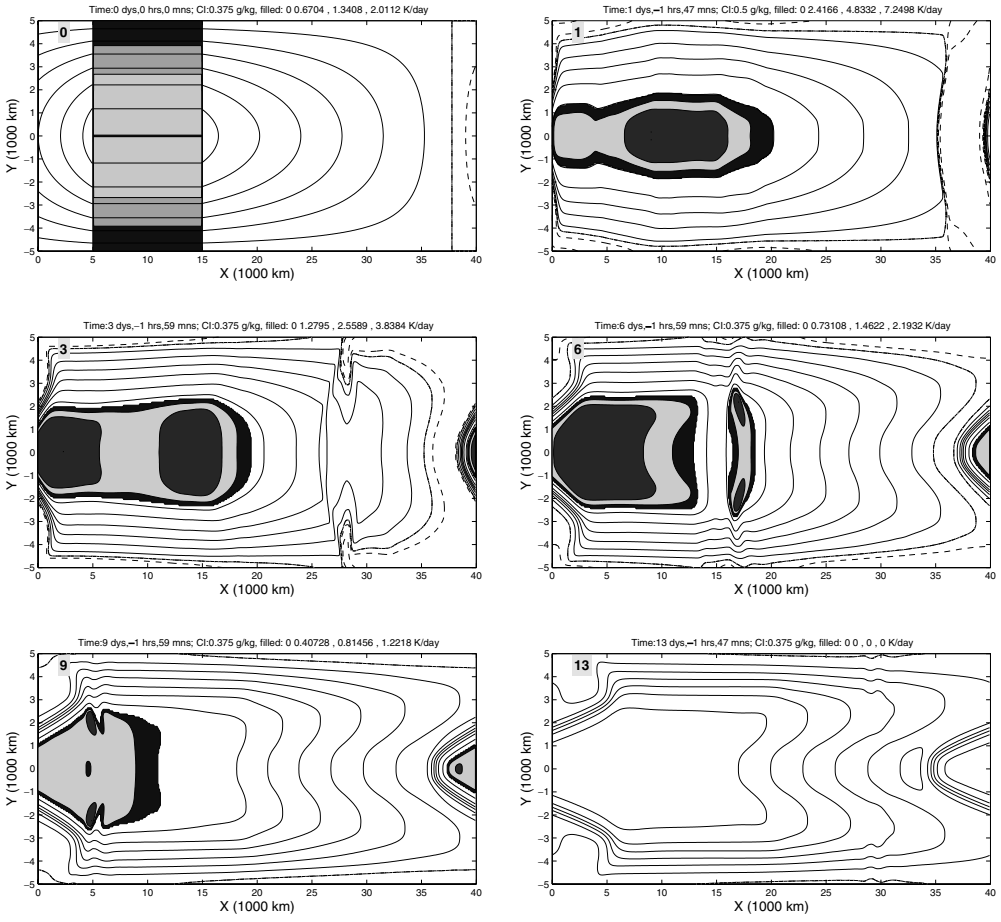

Fig. 9 Contours of the water content, q, (g/kg) and precipitation rate, $\mathcal{P}$, (color filled, K/day) for the dying moisture wave experiment with trade wind barotropic advection. Times $t = 0$, $t = 1$ day, $t = 3$ days, $t = 6$ days, $t = 9$ days, and $t = 13$ days

the distance traveled in one day at a speed of 50 m/s), probably, caused by the reflection of a fast moistening front in a scenario similar to Sect. 7.7 above.

Notice also that at around time $t = 1$ day the precipitation rate attains a maximum peak of close to 8 K/day as depicted in Fig. 8A. Not much is happening between time $t = 1$ day and time $t = 3$ days, except for poleward spread out of the precipitation while its maximum decreases. Nevertheless, we see the shock wave emanating from $x = X$, located between $x = 25,000$ km and $x = 30,000$ km at time $t = 3$ days, approaching toward the moist region. Notice the local peak in the precipitation maximum plot, in Fig. 8A, just before time $t = 6$ days. This is suspected to coincide with the arrival of the dry-shock wave. When the shock hits the moist region, it splits it into two patches of 'active convection', as shown in Fig. 9 at time $t = 6$ days. Later on the two pieces merge together to form again a single convection patch at time $t = 9$ days and continues to decay until the precipitation dissipates away and disappears at about time $t = 13$ days.

3.9 Beta-effect on moisture fronts

We now activate the Coriolis force but switch off the barotropic advection, i.e., we consider the equations in (3.1) (C), (D) and (E) with $\bar{\mathbf{v}} = 0$. The corresponding time histories of energy and precipitation are plotted in Fig. 8B. We see that things have changed and become more complicated. The precipitation maximum displays peaks, that sometimes exceed 10 K/day, with interference by troughs which are sometimes associated with dry episodes of up to 1 day. The time scale of these oscillations varies from about 8 to 12 hours, i.e., longer than the convective characteristic time $\tau_c = 2$ hours. In Fig. 10, we display a few successive snapshots of the flow moisture by drawing the contours of the vertically averaged water content, q, and the color-filled contours of

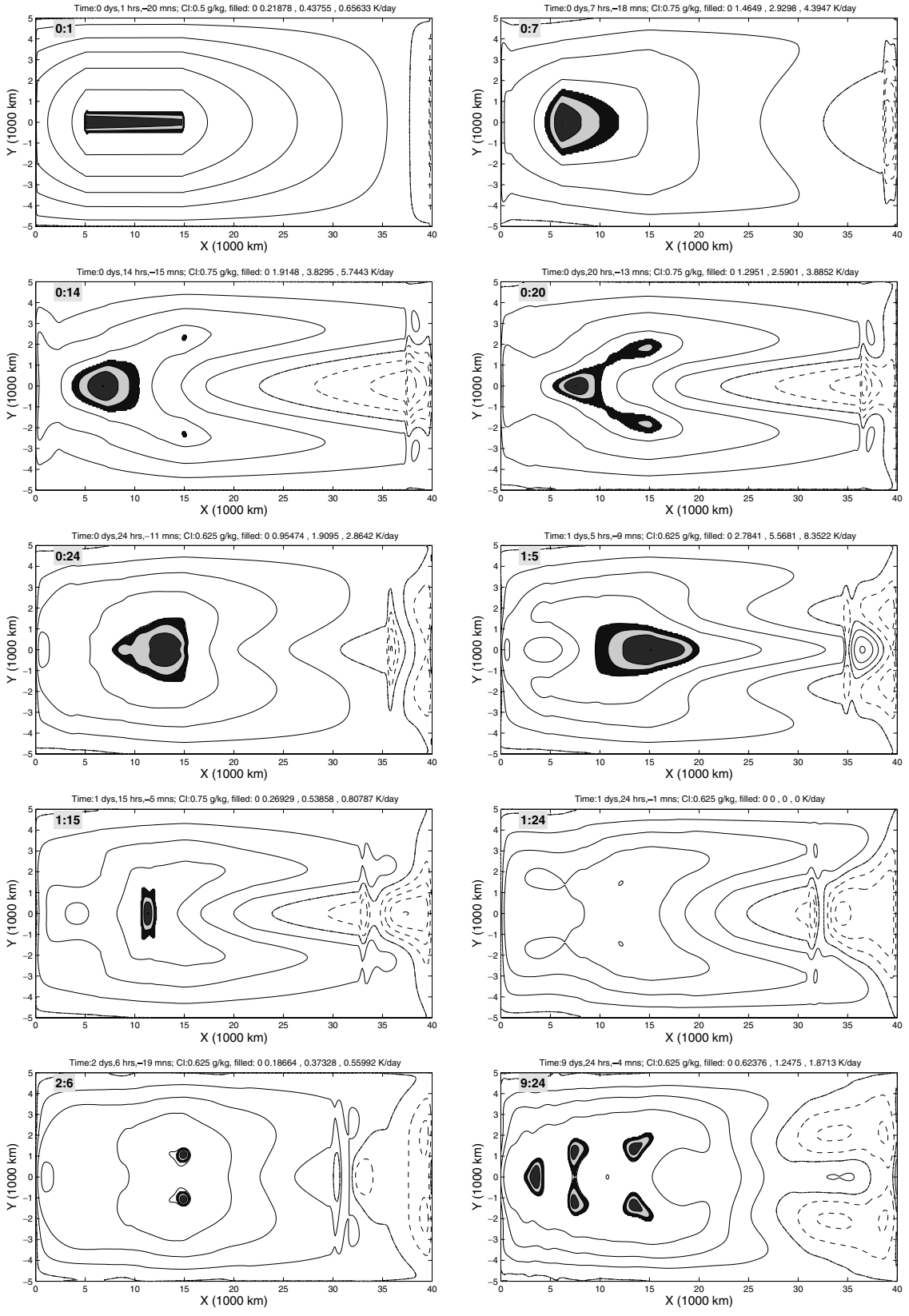

Fig. 10 Same as in Fig. 9 but for the experiment with the beta effect at times 1 hour, 7 hours, 14 hours, 20 hours, 1 day, 1 day and 5 hours, 1 day and 15 hours, 2 days, 2 days and 6 hours, and 10 days

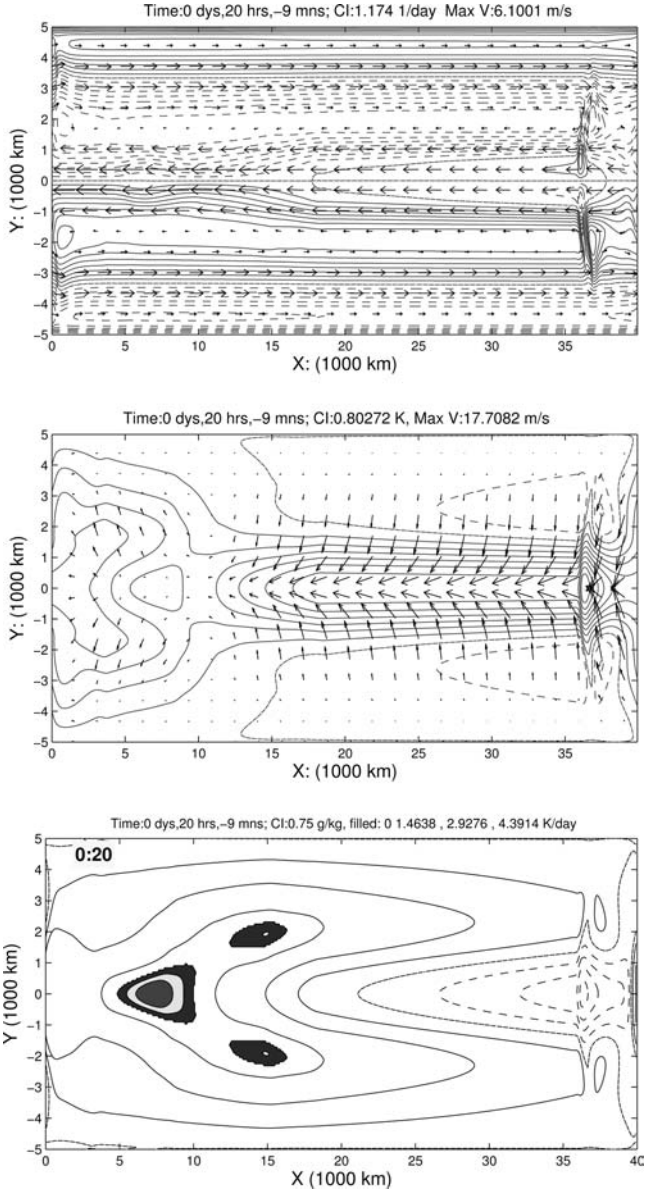

Fig. 11 Profile of the barotropic (*top*) and the baroclinic (*middle*) flows on top of the contours of vorticity and potential temperature, respectively, and contours of the vertically averaged moisture content, q, on top of , color filled contours of the precipitation rate (*bottom*). Experiment with both beta effect and barotropic advection (*trade wind initially*). Time $t = 20$ hours

the precipitation rate, $\mathcal{P}$, on top of them. Clearly, the moisture dynamics are much more complex than in the case without rotation. Perhaps, the most striking phenomenon is the way in which the moisture region deforms and disappears under the beta effect and more excitingly the way in which small islands of precipitation form and merge together. First, we see that the precipitation region, which is initially distributed across the whole channel, quickly shrinks to become a narrow strip centered at the equator as depicted in Fig. 10 at time $t = 1$ hour. Under the effect of rotation the strip elongates poleward while its width diminishes tending to acquire a roundish shape, as shown at time $t = 7$ hours.

This rounding in shape happens while the precipitation maximum increases as suggested by the plot in Fig. 8B. Then suddenly, at time $t = 14$ hours, two small islands starts to form at some distance symmetrically away from the equator. The small islands grow quickly resulting in three patches of precipitation which merge together afterward, at time $t = 20$ hours, to form again a single roundish region which is somewhat located ahead of the one at time $t = 14$ hours. As its front is stretched eastward at the equator, as seen at time $t = 29$

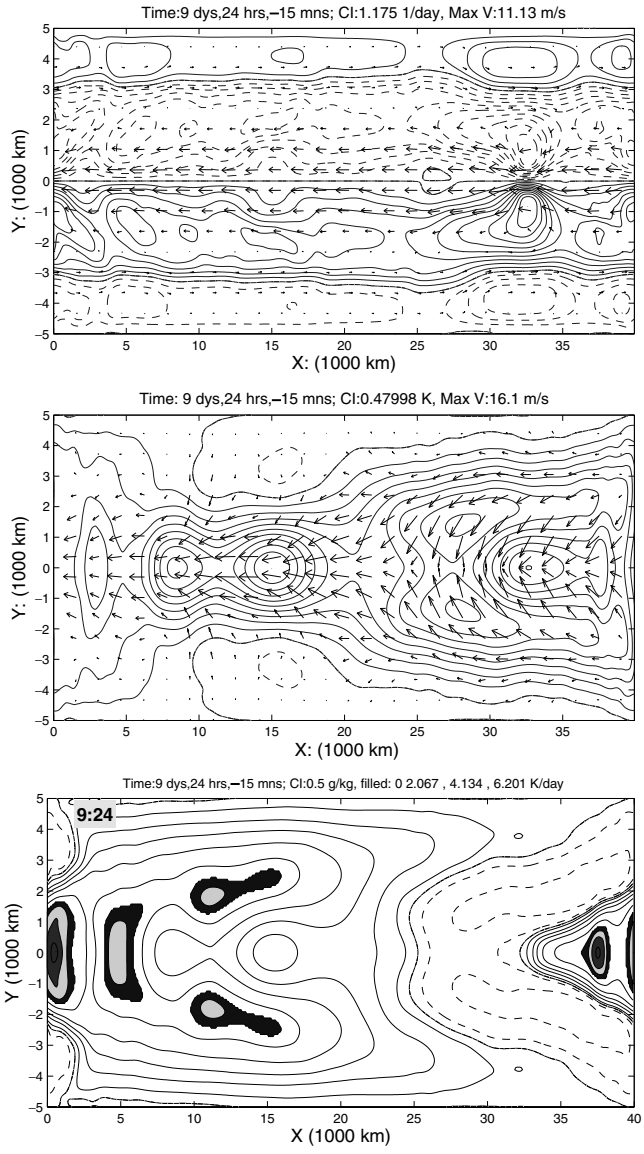

Fig. 12 Same as Fig. 11 but at time $t = 10$ days

hours, it suddenly shrinks backward like a falling spring hitting the ground. This is perhaps due to some effect of the shock wave formed by the boundary condition at $x = X$ and propagating at the dry gravity wave speed toward the moisture wave, reflecting back fast inertia-gravity waves, which are now present in the system with rotation. The structure then becomes a thin stripe oriented north-south as seen at time $t = 39$ hours which then splits onto two pieces and disappears. At time $t = 2$ days we record the first dry episode which lasts about six hours until two islands of precipitation form at some distance off the equator. Interactions with equatorial waves of all kind are suspected to be the main mechanisms underlying the rich dynamics of the precipitation regions.

The dynamics continue under the different scenarios involving formation of small islands of precipitation, growing, merging, deformation, splitting, and finally dissipation. However, at later times the picture seems to be more complex with the co-existence of several islands at once, especially after the dry (shock) wave passes through the moist region and gets smoothed away, as shown on Fig. 10 at time $t = 10$ days.

Finally, it is worth noting from Fig. 8 (panels (a), (b) and (c)) that the energy dissipation during the first few days is much more important for the case without rotation in (b) than it is with the case with rotation in (b) and (c). A simple comparison of the computed total (time integral) dissipation rates,

$D_r = -\int_0^t \int_0^X \int_{-Y}^Y (q - \alpha_c \theta)\mathcal{P}\, dx\, dy\, d\tau$ (see Eq. (3.8)) from panels (a) and (b) reveals that their ratio, $D_r^{(A)}/D_r^{(B)}$, is about 8.1130 for $t = 5$ days and about 7.9214 for $t = 10$ days as it is reflected by the energy curves in Panels A) and B), respectively.

3.10 Beta-effect and barotropic advection simultaneously

Now we put together the effect of rotation and barotropic advection and look at their effect on the precipitation fronts. We run the full coupled system in (3.1) with the initial conditions given by (3.19) for u, v, θ, q, while the barotropic flow at time $t = 0$ is given by the trade wind-like barotropic jet in (3.18) and Fig. 7. Notice that both the barotropic code for the system in Eq. (3.3) of Part I and the baroclinic-barotropic interaction system are activated so that the barotropic shear also undergoes dynamical changes. In Fig. 8C we plot the history of the total energy and of the precipitation maximum associated with this last experiment.

We see clearly that if the moisture dynamics are not more complex than the case with rotation alone, they are at least comparable. Indeed, in Figs. 11 and 12, we plot the structure of the resulting flow at an early time of 20 hours and at a later time of 10 days during the simulation. We see clearly that the moisture plots on the bottom resemble their analogues in Fig. 10, for the case with the beta effect alone, except for some displacement and stretching due to the barotropic flow as experienced above for the case with advection alone. The two top panels on Figs. 11 and 12 display the barotropic (topest panels) and baroclinic (middle panels) flows on top of the vorticity and potential temperature contours, respectively. As the time grows, we see that the barotropic trade wind undergoes interesting changes resulting from its interaction with the baroclinic flow through energy exchange. This is clearly demonstrated by the plots in Fig. 8D, which represent the time histories of the total dry energy $\mathcal{E}_d$ in 1.6) (solid line) and the baroclinic (dash line) and barotropic (dash-dot line) contributions. While the baroclinic and barotropic curves undergo violent and mutually compensating oscillations, their sum (the total dry energy) is relatively smoothly increasing suggesting an extraction of energy from precipitation (the moist energy). Also notice the overall increase in barotropic energy. Indeed, from Figs. 11 and 12, the barotropic wind becomes significantly stronger at the equator, increasing to roughly twice its initial amplitudes, and small scale vortices emerge. The baroclinic flow on the other hand becomes trapped at the equator where a zone of strong convergence appears particularly at and near the precipitation patches. The fluid is strongly sucked toward the equator, hence suggesting a local Hadley-like circulation.

4 Concluding discussion

The overall fractional stepping procedure for the nonlinear barotropic/baroclinic interacting system of Majda and Biello [16], proposed in Part I of this series of papers is tested and applied here for the case of a dry solitary wave and for the interactions with moisture. Recall that the barotropic/baroclinic system is split into three parts involving a shallow water system for the advected baroclinic waves, the incompressible equations for the barotropic flow, and the interaction ODE-system. The resulting subsystems conserve independently their own energy by design, which permits an effective use of the appropriate state of the art non oscillatory/balanced high order methods.

The dry version of the algorithm is tested and applied in Sect. 2 for the barotropic/baroclinic interacting solitary wave of Biello and Majda [16]. It is particularly demonstrated that the numerical scheme developed here was able to capture the strong-nonlinear interactions between the baroclinic and the barotropic components of the flow with little ad hoc dissipation of total energy. This is happening in spite of the apparent formation of small scale structures which are perhaps due to the development of a shear instability after the first few days of evolution. Moreover, it is noticed that, during a short transient period of about two days, before the small scale eddies start to develop, the numerical solution stays close to the asymptotic prediction, when comparing both their spatial structures and their phase speeds. This particularly proves that the two solutions are consistent.

The overall algorithm involving the moisture equation is tested and used in Sect. 3. In order to take advantage of the availability of the precipitation fronts limiting-exact solutions from [17], a simple convective parametrization-like moisture relaxation scheme is used here. Nevertheless, the precipitation front persists for the typical convective time of $\tau_c = 2$ hours as demonstrated in [17] and in Fig. 5. The subsequent tests, adding the effects of a barotropic trade wind and of rotation, have demonstrated the usefulness of the numerical scheme developed here for tropical climate studies and especially the interactions of equatorial waves with

both the midlatitudes and cumulus convection. The results reported in Sect. 3, already, show how rich and complex the interactions of convection with tropical waves can be. First, it is demonstrated that the interaction of a moisture front with a dry gravity wave can either lead to the reflection of a new precipitation front or the complete extinction of the precipitation, depending on the steepness and the strength of the wave itself, as seen in Fig. 6. Unlike the case with advection alone, the beta effect can make patches of precipitation appear at different times and places, merge together to form larger regions of saturated air, and disappear, in an intermittent and chaotic fashion, as demonstrated in Figs. 8–10. This is perhaps due to the capacity of the beta-plane system to support a large diversity of waves. We saw also that the effect of the advection by a barotropic trade wind-like flow is mainly to stretch and displace the moisture patches.

Furthermore, the combination of both the barotropic advection and the beta effect is also an interesting experiment. While the complex dynamics of the precipitation patches induced by the beta effect remained as in the case with rotation alone, the trade wind interacts with the baroclinic moist dynamics and becomes twice as strong through energy exchange at the equator, while small scale vortices are clearly seen at time $t = 10$ days (the top panel of Fig. 12). The other noticeable feature comes from the middle panel of Figs. 11 and 12. We see clearly a strong convergent flow toward the equator suggesting a local Hadley-like circulation, where the air rises at the equator and descends at high latitudes.

Finally, the strategy developed here can easily be generalized to a multi-mode model with a more realistic convective parametrization. Such a generalization is now under investigation in collaboration with other scientists.

Acknowledgements The research of B.K. is supported by a University of Victoria Start-up grant and a grant from the Natural Sciences and Engineering Research Council of Canada. The research of A.M. is partially supported by ONR N0014-96-1-0043, NSF DMS-96225795, and NSF-FRG DMS-0139918.

The authors are thankful to J. Biello for his help in providing the detailed formulas for the solitary waves used in Sect. 2.

Appendix: Algorithm for a two fronts-moisture wave

Here we give the details of the algorithm used to generate the initial data for the moisture runs. We use the index $i = 1, 2, 3$ to denote from left to right the three different regions in Fig. 4. Let

$$u^i = u^i_x x + c^i, \quad \theta^i = \theta^i_x x + d^i, \quad q^i = q^i_x x + e^i \tag{A1}$$

where the slopes X^i_x are such that

$$X^1_x = X_x(a^-), \quad X^2_x = X_x(a^+) = X_x(b^-), \quad X^3_x = X_x(b^+)$$

where X represents u, θ, or q with $u_x = -w$. Suppose that the interface on the left is at $x = a$ and the one on right is at $x = b$. Given the parameters $\tilde{Q}$, α_c, and $\hat{q}$ as in the text, we have the following

Algorithm:

1. Fix the speed, s_a, of drying front (on the left of moist region) such that $c_m \le s_a \le c_d = 1$
2. Fix the vertical velocity within the moist region $w(a^+) = w(b^-)$
3. The vertical velocity in the left dry region is

$$w(a^-) = \left(1 - \frac{K}{1 - s_a^2}\right) w(a^+), \quad K = \frac{\alpha_c + \tilde{Q}}{1 + \alpha_c}$$

4. Fix the speed, s_b, of moistening front (on the right of moist region) such that $0 \le s_b \le c_m$
5. The vertical velocity in the right dry region is

$$w(b^+) = \left(1 - \frac{K}{1 - s_b^2}\right) w(a^+), \quad K = \frac{\alpha_c + \tilde{Q}}{1 + \alpha_c}$$

6. Fix $\theta_x(a^+) = \theta_x(b^-)$, slope of pot. temp. within the moist region
7. The slope of moisture in the moist region satisfies

$$q_x(b^-) = q_x(a^+) = \alpha_c \theta_x(a^+)$$

8. The rest of the slopes follow

$$\theta_x(a^-) = \theta_x(a^+) - s_a(w(a^+) - w(a^-)), \quad \theta_x(b^+) = \theta_x(a^+) + s_b(w(b^+) - w(a^+)),$$

$$q_x(a^-) = q_x(a^+) - \left(\frac{1-\tilde{Q}}{s_a} - s_a\right)(w(a^+) - w(a^-)),$$

$$q_x(b^+) = q_x(a^+) + \left(\frac{1-\tilde{Q}}{s_b} - s_b\right)(w(b^+) - w(a^+))$$

References

1. Majda, A., Biello, J.: The nonlinear interaction of barotropic and equatorial baroclinic Rossby waves. J. Atmos. Sci. **60**, 1809–1821 (2003)
2. Biello, J., Majda, A.: Boundary layer dissipation and the nonlinear interaction of equatorial baroclinic barotropic Rossby waves. Geophysical and Astrophysical Fluid Dynamics **98**, 85–127 (2004)
3. Webster, P.: Response of the tropical atmosphere to local steady forcing. Mon. Wea. Rev. **100**, 518–541 (1972)
4. Webster, P.: Mechanisms determining the atmospheric response to sea surface temperature anomalies. J. Atmos. Sci. **38**, 554–571 (1981)
5. Webster, P.: Seasonality in the local and remote atmospheric response to sea surface temperature anomalies. J. Atmos. Sci. **39**, 41–52 (1982)
6. Kasahara, A., Silva Dias, P.: Response of planetary waves to stationary tropical heating in a global atmosphere with meridional and vertical shear. J. Atmos. Sci. **43**, 1893–1911 (1986)
7. Hoskins, B., Jin, F.-F.: The initial value problem for tropical perturbations to a baroclinic atmosphere. Quart. J.Roy. Meteor. Soc. **117**, 299–317 (1991)
8. Wang, B., Xie, X.: Low-frequency equatorial waves in vertically sheared zonal flow. Part I: Stable waves. J. Atmos. Sci. **53**, 449–467 (1996)
9. Chiang, J., Sobel, A.: Tropical tropospheric temperature variations caused by ENSO and their influence on the remote tropical climate. J. Atmos. Sci. **15**, 2616–2631 (2002)
10. Emanuel, K.: An air-sea interaction model of intraseasonal oscillations in the tropics. J. Atmos. Sci. **44**, 2324–2340 (1987)
11. Neelin, D., Held, I., Cook, K.: Evaporation-wind feedback and low frequency variability in the tropical atmosphere. J. Atmos. Sci. **44**, 2341–2348 (1987)
12. Goswami, P., Goswami, B.: Modification of $n = 0$ equatorial waves due to interaction between convection and dynamics. J. Atmos. Sci. **48**, 2231–2244 (1991)
13. Yano, J.-I., Emanuel, K.: An improved model of the equatorial troposphere and its coupling to the stratosphere. J. Atmos. Sci. 377–389 (1991)
14. Neelin, D., Yu, J.: Modes of tropical variability under convective adjustment and the Madden-Julian Oscillation. Part I: Analytical theory. J. Atmos. Sci. **51**, 1876–1894 (1994)
15. Majda, A., Shefter, M.: Waves and instabilities for model tropical convective parametrizations. J. Atmos. Sci. **58**, 896–914 (2001)
16. Biello, J., Majda, A.: The effect of meridional and vertical shear on the interaction of equatorial baroclinic and barotropic Rossby waves. Studies in App. Math. **112**, 341–390 (2003)
17. Frierson, D., Majda, A., Pauluis, O.: Dynamics of precipitation fronts in the tropical atmosphere. Comm. Math. Sciences **2**(4) (2004)
18. Bale, D., LeVeque, R., Mitran, S., Rossmanith, J.: A wave propagation method for conservation laws and balance laws with spatially varying flux functions. SIAM Jour. Sci. Comput. **24**, 955–978 (2002)
19. Levy, D., Tadmor, E.: Non-oscillatory central schemes for the incompressible 2-D Euler equations. Mathematical Research Letters **4**, 1–20 (1997)
20. Majda, A.: Introduction to PDEs and Waves for the Atmosphere and Ocean. Courant Lecture Notes, vol. 9. Amer. Mat. Soc. (2003)
21. Gill, A.: Atmosphere-Ocean Dynamics. International Geophysics Series, vol. 30. Academic Press (1982)
22. Zehnder, J.: A comparison of convergence- and surface-flux-based convective parametrizations with applications to tropical cyclogenesis. J. Atmos. Sci. **58**, 283–301 (2001)
23. Neelin, D., Zeng, N.: A quasi-equilibrium tropical circulation model–formulation. J. Atmos. Sci. **57**, 1741–1766 (2000)
24. Wheeler, M., Kiladis, G.: Convectively coupled equatorial waves: Analysis of clouds and temperature in the wavenumber-frequency domain. J. Atmos. Sci. **56**, 374–399 (1999)
25. Emanuel, K.: Atmospheric Convection. Oxford University Press (1994)
26. Lax, P.: Hyperbolic systems of conservation laws II. Comm. Pure Appl. Math. **10**, 537–566 (1957)
27. Majda, A.: The stability of multi-dimensional shock fronts. Mem. Amer. Math. Soc. vol. 41. Amer. Math. Soc. (1983)
28. LeVeque, R.: Balancing source terms and flux gradients in high-order Godunov methods: The quasi-steady wave-propagation algorithm. J. Comput. Phys. **146**, 346–365 (1998)
29. LeVeque, R.: Numerical Methods for Conservation Laws. Birkhäuser, Basel (1990)